International Journal of Heat and Fluid Flow 29 (2008) 591–601

Contents lists available at ScienceDirect

International Journal of Heat and Fluid Flow

journal homepage: www.elsevier.com/locate/ijhff

Spatio-temporal turbulent structures of thermal boundary layer subjected to non-equilibrium adverse pressure gradient

T. Houra [a,*], Y. Nagano [b]

[a] Department of Environmental Technology, Nagoya Institute of Technology, Gokiso-cho, Showa-ku, Nagoya 466-8555, Japan
[b] Department of Mechanical Engineering, Nagoya Institute of Technology, Nagoya, Japan

ARTICLE INFO

Article history:
Received 11 November 2007
Received in revised form 5 March 2008
Accepted 8 March 2008
Available online 22 April 2008

Keywords:
Turbulent boundary layer
Heat transfer
Adverse pressure gradient
Hot- and cold-wire measurement
Proper orthogonal decomposition

ABSTRACT

We have experimentally investigated a non-equilibrium turbulent boundary layer subjected to an adverse pressure gradient developing on a uniformly heated flat wall. The spatio-temporal structures educed from a multi-point simultaneous measurement are reasonably interpolated based on the "proper orthogonal decomposition (POD)". In the near-wall region, elongated hot regions stay dull and less active, whereas, large-scale cold regions having strong energy frequently intrude into the near-wall region. The energy-containing events in the near-wall region are discussed based on the results of wavelet analysis.

1. Introduction

Characteristics of turbulent boundary layer flows with adverse pressure gradients (APG) differ significantly from those of canonical boundary layers. Among previous studies, the experimental investigations conducted by Clauser (1954), Bradshaw (1967) and the theoretical one by Rotta (1962) are well-known with regard to the equilibrium boundary layer (with the pressure gradient parameter kept constant). The equilibrium APG boundary layer has produced some interest in the statistical features of self-similarity, and is thus the subject of experiments (Skåre and Krogstad, 1994) and direct numerical simulations (DNS) (Skote et al., 1998). In actual flow fields, however, the equilibrium condition is not necessarily satisfied, and the various characteristics of turbulent boundary layer flows may emerge from more general conditions. For example, the development of a turbulent boundary layer after a sudden change in external conditions (Townsend, 1976) is typical. Thus, many researchers have been investigating the boundary layers under non-equilibrium pressure gradient conditions. Research on non-equilibrium APG boundary layers has been conducted both experimentally (Samuel and Joubert, 1974; Nagano et al., 1993, 1998; Houra et al., 2000; Indinger et al., 2006) and numerically (Spalart and Watmuff, 1993; Na and Moin, 1996; Coleman et al., 2003; Lee and Sung, 2007).

With respect to the heat transfer characteristics in APG boundary layers, classical experimental data under an equilibrium APG condition (Blackwell et al., 1972) are still used in order to validate proposed turbulence models and/or theory (Bradshaw and Huang, 1995; Volino and Simon, 1997; Wang et al., 2008). Thus, in order to improve the model predictions for practical usage, we must elucidate non-equilibrium APG effects on turbulent boundary layers with heat transfer.

From our previous heat transfer experiment on a non-equilibrium APG turbulent boundary layer (Houra and Nagano, 2006), we obtained the following results: (1) the standard log-law for both velocity and temperature profiles in a zero-pressure gradient (ZPG) boundary layer does not hold in APG boundary layers; (2) the Stanton number follows the correlation curve for ZPG flows, although the corresponding skin friction coefficient decreases drastically; and (3) both the ejection and sweep motions contribute significantly to the heat transport in APG flows, though sweep motions with shorter durations are the main contributor to the momentum transfer. It means that the effects of APG on the thermal field are not similar to those on the velocity field. In this situation, it is not resolved why the dissimilarity between the momentum and heat transports occurs. In order to settle the issue, we need to elucidate the spatio-temporal structures of turbulent heat transfer in non-equilibrium APG flows.

In this paper, multi-point simultaneous measurements of velocity and thermal fields are introduced to investigate the effect of the non-equilibrium APG on the interaction between large-scale motions in the outer layer and small-scale coherent structures near

* Corresponding author. Tel./fax: +81 52 735 7795.
E-mail address: houra@heat.mech.nitech.ac.jp (T. Houra).

0142-727X/$ - see front matter © 2008 Elsevier Inc. All rights reserved.
doi:10.1016/j.ijheatfluidflow.2008.03.004

Nomenclature

a	scaling parameter, $a = 1/f$
C_p	wall static pressure coefficient, $C_p = (\overline{P} - \overline{P}_0)/(\rho \overline{U}_0^2/2)$
c_p	specific heat at constant pressure
C_ψ	admissibility constant
$E_{XY}(a,t)$	local wavelet spectrum
f	frequency
f'	dimensionless frequency, $f' = f\tau_E$
$\overline{P}$	mean pressure
P^+	dimensionless pressure gradient parameter, $P^+ = \nu(\mathrm{d}\overline{P}/\mathrm{d}x)/\rho u_\tau^3$
$\overline{P}_0$	reference inlet pressure
Pr	Prandtl number
q_w	heat flux at wall
$R_{u\theta}$	correlation coefficient between u and θ
$R_{v\theta}$	correlation coefficient between v and θ
R_{Δ_2}	Reynolds number based on enthalpy thickness, $R_{\Delta_2} = \overline{U}_e \Delta_2/\nu$
R_{δ_2}	Reynolds number based on momentum thickness, $R_{\delta_2} = \overline{U}_e \delta_2/\nu$
St	Stanton number, $St = q_w/(\rho c_p \overline{U}_e \overline{\Theta}_e)$
T	temperature
$\overline{T}_e, \overline{T}_w$	ambient and wall temperatures
t	time
$\overline{U}$	mean velocity in x direction
$\overline{U}_e$	free-stream velocity
$\overline{U}_0$	reference inlet velocity
u, v	fluctuating velocity components in x and y directions
u_τ	friction velocity, $u_\tau = \sqrt{\tau_w/\rho}$
x, y, z	streamwise, wall-normal and spanwise coordinates
y^+	dimensionless distance from wall, $y^+ = u_\tau y/\nu$

Greek symbols

β	Clauser pressure gradient parameter, $\beta = (\delta_1/\tau_w)\mathrm{d}\overline{P}/\mathrm{d}x$
Δ	thickness of thermal boundary layer
Δ_2	enthalpy thickness of thermal boundary layer
δ	thickness of momentum boundary layer
δ_1, δ_2	displacement and momentum thicknesses of boundary layer
$\overline{\Theta}$	temperature difference from wall, $\overline{\Theta} = \overline{T}_w - \overline{T}$
$\overline{\Theta}^+$	temperature difference normalized by friction temperature, $\overline{\Theta}^+ = \overline{\Theta}/\theta_\tau$
$\overline{\Theta}_e$	temperature difference between wall and ambient, $\overline{\Theta}_e = \overline{T}_w - \overline{T}_e$
θ	fluctuating temperature difference, $\theta = \Theta - \overline{\Theta} = \overline{T} - T$
θ_τ	friction temperature, $\theta_\tau = q_w/(\rho c_p u_\tau)$
ν	kinematic viscosity
ρ	density
τ_E	Taylor time scale or Eulerian dissipation time scale, $\tau_E = \sqrt{2\overline{u^2}/\overline{(\partial u/\partial t)^2}}$
τ_w	wall shear stress
ψ	analyzing wavelet

Subscript and superscripts

0	reference inlet point
$\overline{()}$	time mean value
$()^+$	normalization by inner variables (u_τ, ν)
$\hat{()}$	normalization by r.m.s. value
$(^*)$	complex conjugate

the wall. An array of five identical three-wire probes, each composed of an X-type hot wire and a fine cold-wire, is aligned in the wall-normal direction to measure simultaneously the velocity and thermal fields. From the measured velocity components in the streamwise and wall-normal directions and relevant temperature, the turbulent heat transfer field can be interpolated using the "proper orthogonal decomposition (POD)" for spatially interpolating the data. Then, the energy-containing events in the near-wall region are discussed based on the results of wavelet analysis.

2. Experimental apparatus

The experimental apparatus used is the same as described in our previous studies (Nagano et al., 1993, 1998; Houra et al., 2000; Houra and Nagano, 2006). The working fluid is air ($Pr = 0.71$). For the heat transfer experiment, a flat plate, on which a turbulent boundary layer develops, is constructed with the 2-mm thick copper plate and a.c. heated from the back of the plate. The wall temperature distribution is monitored through embedded thermocouples and kept uniform during the experiment. The test section is composed of the heated flat plate and a roof-plate to adjust pressure gradients (see Nagano et al., 1993, 1998). The aspect ratio at the inlet to the test section is 13.8 (50.7 mm high × 700 mm wide). Under the present measurement conditions, the free-stream turbulence level is below 0.1%. To generate a stable turbulent boundary layer, a row of equilateral triangle plates is located at the inlet to the test section as a tripping device. The important flow parameters are listed in Table 1. In the APG flow, the pressure gradient $\mathrm{d}Cp/\mathrm{d}x$ keeps a nearly constant value of 0.6 m^{-1} over the region 65 mm $\leqslant x \leqslant$ 700 mm, and then decreases slowly (x is the streamwise distance from a tripping point). The pressure gradient parameter normalized by inner variables P^+ and the Clauser parameter β increase with increasing x, thus yielding moderate to strong APG. The Reynolds number increases with increasing x even in ZPG flows. However, the effect of the Reynolds number on turbulent flows is small compared with that of APG (Nagano et al., 1993). Thus, the following discussion is based on the variation in P^+. In order to eliminate buoyancy effects, a small temperature difference was required experimentally. However, if the difference is too small, the temperature sensor resolution would be insufficient. Thus, we maintained a temperature difference of about 10 K between the wall and ambient fluid when using a low-noise high-gain instrumentation amplifier and 14-bit A/D connection. The variation in the wall temperature over the test section is within ±0.5 K of the mean.

Table 1
Flow parameters ($\overline{U}_0 = 10.8$ m/s, $\overline{\Theta}_e = 10$ K)

x (mm)	$\overline{U}_e$ (m/s)	δ (mm)	Δ (mm)	R_{δ_2}	R_{Δ_2}	P^+	β
935 (ZPG)	10.8	19.9	21.0	1620	1920	0	0
535 (APG)	9.1	16.2	19.4	1330	1160	0.91×10^{-2}	0.77
735 (APG)	8.3	24.6	25.3	1930	1280	1.93×10^{-2}	2.19
935 (APG)	7.6	34.2	37.1	2730	1730	2.56×10^{-2}	3.95

Velocity and temperature fluctuations were simultaneously measured by the specially devised hot- and cold-wire technique (Hishida and Nagano, 1978; Nagano and Tsuji, 1994). The probe consisted of three fine wires, the upstream wire serving as the constant current cold-wire (platinum 90%/ rhodium 10%; diameter 0.625 μm; length 1.0 mm ≃ 18 in wall units; length-to-diameter ratio is 1600), and the two symmetrically bent V-shaped hot wires (Hishida and Nagano, 1988a,b; tungsten; diameter 5 μm; length 0.8 mm). The spatial resolution of the three-wire probe in the wall-normal direction is about 0.3 mm. The first measurement

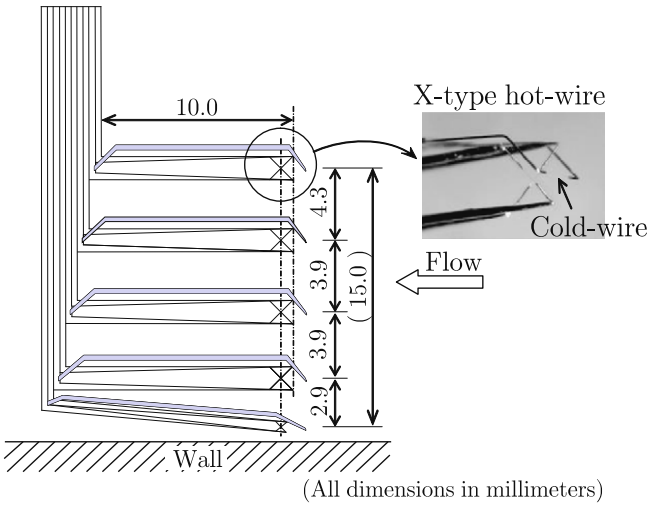

Fig. 1. Array of five X-I probes for multi-point simultaneous measurement.

point was found to be located 0.6 mm from the wall, from examining the reliability of the data (Tagawa et al., 1992). An array of five identical three-wire probes, each composed of an X-type hot wire and a fine cold-wire, is aligned in the wall-normal direction for simultaneous measurement, as shown in Fig. 1. The shape of this array is designed to measure the velocity and thermal fields simultaneously, where the effects of APG become significant, i.e., the buffer region (the sensor closest to the wall): $y^+ = 20.7$ ($y/\delta \simeq 0.04$), two locations in the log region: $y^+ = 68.3$ ($y/\delta \simeq 0.12$), $y^+ = 131.6$ ($y/\delta \simeq 0.24$), the outer edge of the log region: $y^+ = 192.6$ ($y/\delta \simeq 0.35$), and the outer layer (the sensor farthest from the wall): $y^+ = 263.0$ ($y/\delta \simeq 0.48$). The two velocity components in the streamwise and wall-normal directions and temperature are measured simultaneously, and a set of each data at different y values from the measurement points is interpolated using the proper orthogonal decomposition (Houra et al., 2000). To convert the hot wire outputs into the velocity components, we used the well-established look-up-table method (Lueptow et al., 1988). Also, the bias error, which is ascribed to the spatial separation of the two wires of an X-probe, was removed in accordance with the procedure indicated by Tagawa et al. (1992).

3. Results and discussion

3.1. Principal aspects of APG flow

Before discussing the near-wall turbulent structures in detail, we summarize the principal aspects of the APG flow in the following. In the present study, the pressure distribution does not preserve the equilibrium condition (i.e., $\beta \neq$ const.); thus, the mean velocity profile in an APG flow develops in such a way as to increase the thickness of the layer and the shape factor.

With increasing P^+, the defect in the mean velocity $\overline{U}$ from the free-stream velocity $\overline{U}_e$ becomes larger as shown in Fig. 2. Thus, in the outer coordinates, the mean velocity profile does not maintain self-similarity under the non-equilibrium condition. On the other hand, if the mean velocity is normalized by the friction velocity u_τ, the velocity profiles in APG flows lie below the following 'standard' log-law profile for ZPG flows:

$$\overline{U}^+ = 2.44 \ln y^+ + 5.0 \quad (1)$$

as shown in Fig. 3 (for detail see Nagano et al., 1993, 1998). This important characteristic of the APG flows is also confirmed by the DNS of Spalart and Watmuff (1993) and by the measurement of

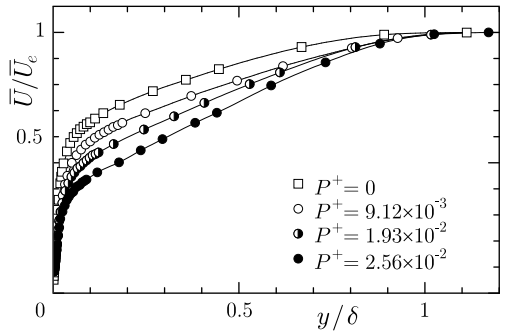

Fig. 2. Mean velocity profiles in ZPG and APG flows in outer coordinates.

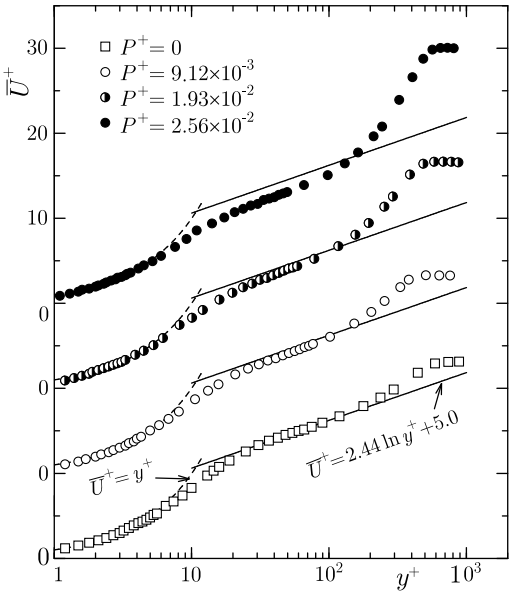

Fig. 3. Mean velocity profiles in ZPG and APG flows in wall coordinates.

Debisschop and Nieuwstadt (1996). Moreover, this finding is corroborated by the DNS for an APG recovery region of a backward-facing step flow (Le et al., 1997). More recent DNS (Lee and Sung, 2007) and measurement (Indinger et al., 2006) also ensure that the law of the wall does not hold in this condition.

The intensity profiles of fluctuating velocity components, u and v, normalized by the free-stream velocity, $\overline{U}_0$, at the inlet to the test section, are presented in Fig. 4. The abscissa is the distance from the wall normalized with the boundary layer thickness, δ. With an increasing APG effect, the reduction in turbulence intensities can be seen in the wall region ($y/\delta < 0.4$), whereas all the profiles in the outer layer are kept unchanged. Thus, turbulence intensities are considered to be unchanged along the streamlines of the mean flow lying outside the wall region, since the streamlines and the lines of constant y/δ are approximately the same (Nagano et al., 1993, 1998). On the other hand, if the turbulent intensities in APG flows are normalized by the friction velocity, u_τ, all of the velocity fluctuation components become remarkably large in the outer region of the APG boundary layers (Nagano et al., 1993).

Fig. 5 shows the mean temperature profiles normalized by the temperature difference between the wall and the ambient, $\overline{\Theta}/\overline{\Theta}_e[= (\overline{T}_w - \overline{T})/(\overline{T}_w - \overline{T}_e)]$. The abscissa is the distance from the wall normalized by the 99% thickness of the thermal boundary layer. As clearly seen from this figure, there are few effects of APG on the mean temperature profiles on the basis of this normalization (Houra and Nagano, 2006). However, if we normalize the

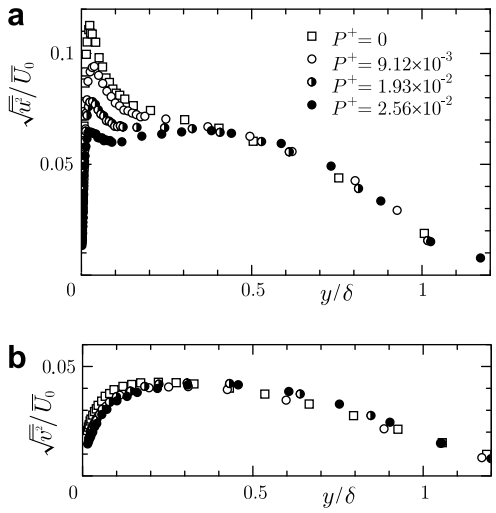

Fig. 4. Turbulence intensities of fluctuating velocity components: (a) streamwise; (b) wall-normal.

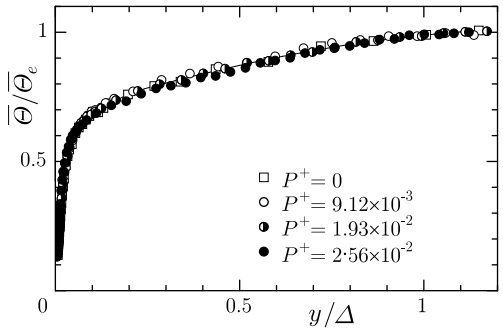

Fig. 5. Mean temperature profiles in ZPG and APG flows in outer coordinates.

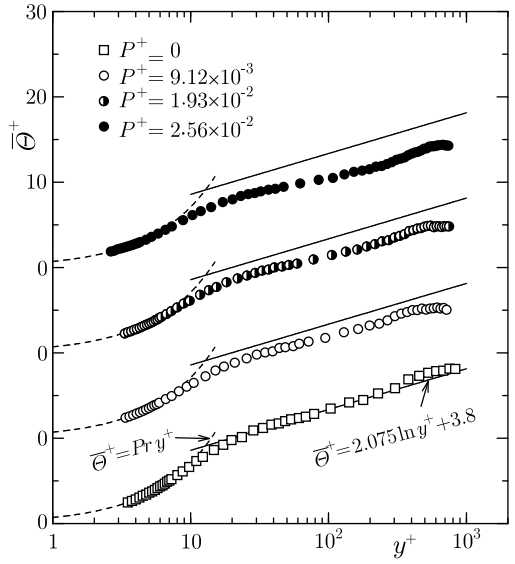

Fig. 6. Mean temperature profiles in ZPG and APG flows in wall coordinates.

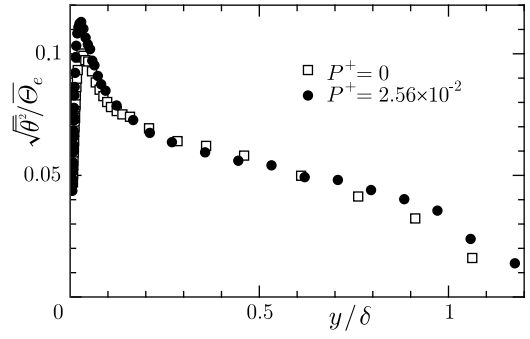

Fig. 7. r.m.s. profiles of temperature fluctuations in ZPG and APG flows.

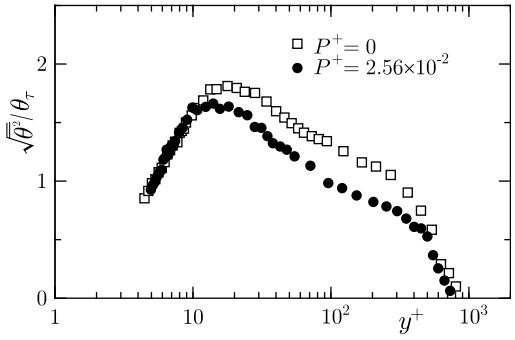

Fig. 8. r.m.s. profiles of temperature fluctuations in ZPG and APG flows in wall coordinates.

mean temperature by the wall unit, the temperature profiles in the APG flow lie below the universal log-law profiles for ZPG thermal boundary layer:

$$\overline{\Theta}^+ = Pr\,y^+, \quad \overline{\Theta}^+ = 2.075\ln y^+ + 3.8, \tag{2}$$

and the increase in the wake region disappears, as compared with the mean velocity profiles of APG flows (see Figs. 3 and 6). The important characteristics of APG flows conform to previously reported experimental results in equilibrium APG flows (Perry et al., 1966; Blackwell et al., 1972) and well correspond to the theoretical conjecture of Bradshaw and Huang (1995), i.e., the law of the wall for a thermal field is more affected by pressure gradient than that for a velocity field. It should be noted that this reduction in the mean temperature at the outer edge of the layer, i.e., $\overline{\Theta}_e^+ (= \sqrt{C_f/2}/St)$, is mainly due to the reduction in the skin friction coefficient, because the Stanton number is unaffected by imposing an APG (Houra and Nagano, 2006).

Figs. 7 and 8 show the r.m.s. amplitude of temperature fluctuations, normalized by the temperature difference, $\overline{\Theta}_e$, and that normalized by the friction temperature, θ_τ, respectively. As seen from Fig. 7, there is little effect on the raw values of temperature fluctuation intensities. On the other hand, if we normalize the intensity by the friction temperature, the intensity decreases by imposing the APG as shown in Fig. 8. This tendency is opposite to that in the intensities of velocity fluctuation, i.e., the r.m.s. intensities of velocity fluctuations normalized by the friction velocity apparently increase (Nagano et al., 1993). Thus, the law of the wall for the temperature fluctuation also does not hold in the APG flows.

In the following, we revisit the unique features of turbulent shear stress and heat flux (Houra and Nagano, 2006). Fig. 9 shows the profiles of the Reynolds shear stress, $-\overline{uv}$, normalized by the friction velocity, u_τ. The abscissa is the distance from the wall normalized by the 99% thickness of the boundary layer, δ. It includes the experimental and numerical results in ZPG flows (Verriopoulos, 1983; Spalart, 1988). With increasing P^+, $-\overline{uv}/u_\tau^2$ drastically increases in the outer region. Thus, the constant-stress layer relationship $-\overline{uv}/u_\tau^2 \simeq 1$ observed in the ZPG flows is no longer valid. This, too, may account for the non-existence of the universal law of the wall in APG boundary layers (see Fig. 3).

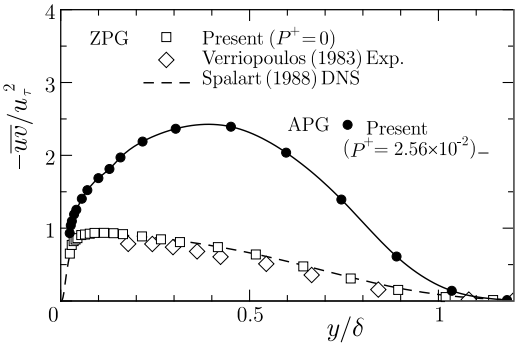

Fig. 9. Reynolds shear stress in ZPG and APG flows.

Fig. 10 shows the wall-normal turbulent heat flux, $-\overline{v\theta}$, normalized by the friction velocity, u_τ, and temperature, θ_τ, in ZPG and APG flows. The fluctuating temperature difference, θ, is defined as $\theta = \Theta - \overline{\Theta} = \overline{T} - T$. Thus, $\theta < 0$ indicates hotter than the mean temperature, and $\theta > 0$ colder. As seen from Fig. 10, the wall-normal turbulent heat flux in APG flow is kept unchanged over the entire region compared with the Reynolds shear stress in Fig. 9.

As previously shown in Fig. 7, the raw values of temperature fluctuation intensities hardly change in APG flow, though the streamwise velocity fluctuation affected by APG decreases in the near-wall region as seen from Fig. 4a. Thus, the streamwise turbulent heat flux $\overline{u\theta}$ normalized by the constant reference velocity, $\overline{U}_0$, and temperature difference, $\overline{\Theta}_e$, decreases in the near-wall region of APG flow, in comparison with ZPG flow (not shown here). Fig. 11a shows the correlation coefficients between streamwise velocity and temperature fluctuations, $R_{u\theta}$. In the ZPG flow, the correlation coefficient stays as high as 0.6 in the outer layer, and approaches unity at the wall (Antonia et al., 1988). On the other hand, in the APG flow, although a reduction in the correlation can be seen, it remains as high as 0.55 over most of the layer. Thus, in the APG flow, it might be expected that the streamwise velocity and temperature fluctuations are still closely related to each other, as in the canonical wall flow. However, the slight reduction in $R_{u\theta}$ is due to the increase of the inactive low-frequency motions, which are caused by the imposing APG (Nagano and Houra, 2002).

To clarify the effects of APG on the wall-normal heat flux, we decompose the turbulent heat flux into the product of the correlation coefficient and the relevant intensities:

$$\frac{-\overline{v\theta}}{u_\tau\theta_\tau} = \frac{-\overline{v\theta}}{\sqrt{\overline{v^2}}\sqrt{\overline{\theta^2}}}\frac{\sqrt{\overline{v^2}}}{u_\tau}\frac{\sqrt{\overline{\theta^2}}}{\theta_\tau} = -R_{v\theta}\frac{\sqrt{\overline{v^2}}}{u_\tau}\frac{\sqrt{\overline{\theta^2}}}{\theta_\tau}.$$

The correlation coefficient, $R_{v\theta}$, hardly changes in APG flows as shown in Fig. 11b. The correlation coefficient, $R_{v\theta}$, is determined

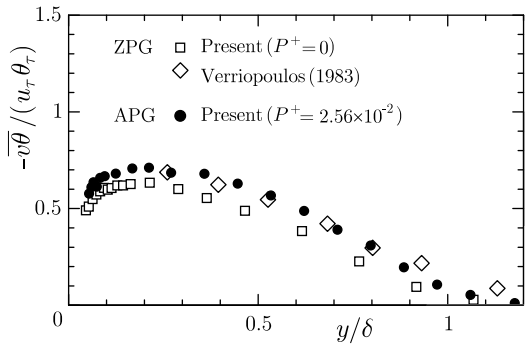

Fig. 10. Wall-normal turbulent heat flux in ZPG and APG flows.

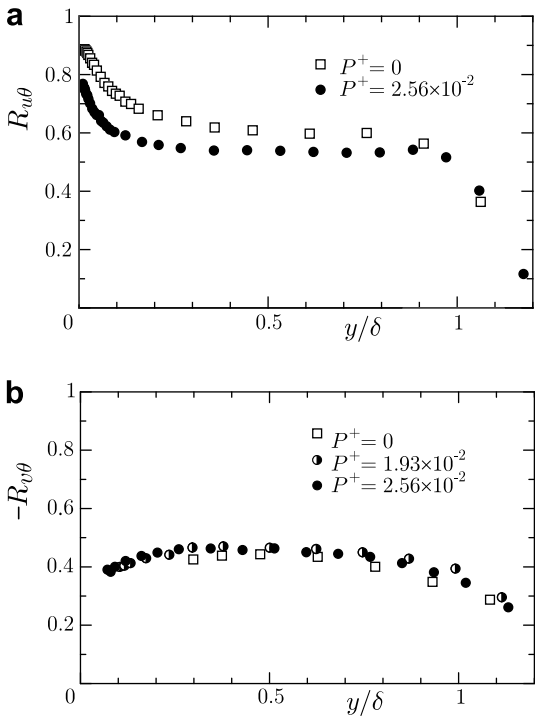

Fig. 11. Correlation coefficients between each velocity component and temperature fluctuation in ZPG and APG flows: (a) $R_{u\theta}$; (b) $-R_{v\theta}$.

by the motions at higher-frequency than the correlation coefficient, $R_{u\theta}$. The higher-frequency motions are unaffected by imposing APG, as shown by the bispectrum measurement (Nagano and Houra, 2002). Thus, this could be the reason why the correlation coefficient between v and θ is maintained.

While the normalized intensity of velocity fluctuations by the friction velocity increases (Nagano et al., 1993), that of the temperature fluctuation by the friction temperature decreases (see Fig. 8). Thus, the effects of APG on these normalized intensities act in opposite directions, and this results in the little change in the normalized turbulent heat flux as shown in Fig. 10. It should be noted that the normalization by the friction velocity and temperature means the normalization by the wall-normal heat flux at the wall divided by the density and the specific heat at constant pressure, i.e., $u_\tau\theta_\tau = q_w/(\rho c_p)$. Because the pressure gradient term does not appear in the energy equation, the total heat flux, i.e., the conduction plus turbulent heat flux, is maintained at a constant level near the wall. Thus, the effects on the wall-normal turbulent heat flux should be small in APG flow. Moreover, from the viewpoint of turbulent transport, because the heat transfer is determined with the wall-normal motions, little effect of APG on the wall-normal velocity component (see Fig. 4b) results in correspondingly little change in the thermal field.

3.2. Waveforms in the near-wall region of APG flow

Fig. 12 shows the instantaneous signal traces of streamwise and wall-normal velocities, $\hat{u}$ and $\hat{v}$, and temperature fluctuations, $\hat{\theta}$, together with the second- and third-order moments, in the buffer region of the APG flow. The circumflex $\hat{}$ denotes the normalization by the respective r.m.s. value. The abscissa is the time normalized by the Taylor time scale, τ_E. The normalized period of about 10 in the Taylor time scale corresponds to the mean period of the intermittent bursts (Nagano et al., 1998). The two shaded regions labeled (a) and (b), respectively, correspond to the time periods in Fig. 14a and b, as will be discussed later.

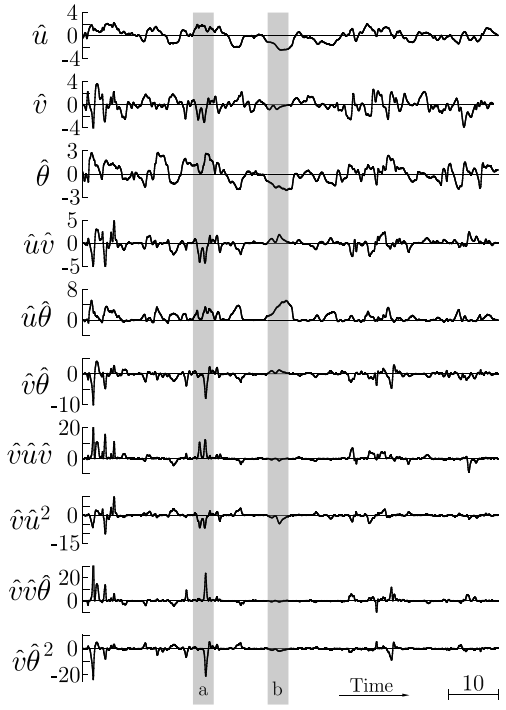

Fig. 12. Velocities and temperature signal traces in APG flow, with time being normalized by Taylor time scale τ_E ($y^+ = 20.7$, $y/\delta = 0.04$).

As seen from Fig. 12, at the time period (a), the sweep motions ($Q4$: $u > 0$, $v < 0$) largely contribute to the Reynolds shear stress, $-\hat{u}\hat{v}$, and the wall-normal heat flux, $-\hat{v}\hat{\theta}$. Moreover, very large-amplitude fluctuations of $\hat{v}\hat{u}\hat{v}$ and $\hat{v}\hat{u}^2$, are respectively skewed to the positive and negative sides, besides which the large-amplitude outward interactions ($Q1$: $u > 0$, $v > 0$) are associated with the $Q4$ motions. These facts indicate that the $Q4$ motions are the principal contributor here.

On the contrary, the ejection motions ($Q2$: $u < 0$, $v > 0$) occur much less frequently than the $Q4$ motions. This is quite opposite to what occurs in ZPG flows (Houra et al., 2000). For example, before and after the time period (a), the contributions to $-\hat{u}\hat{v}$ and $-\hat{v}\hat{\theta}$ from the $Q2$ motions are much smaller than that from the $Q4$ motions. Moreover, the $Q2$ motions have small amplitude in the wall-normal velocity and their durations become longer. The important characteristics in the duration and frequency of the events have been examined by the ensemble averaged waveforms and their occurrence based on the trajectory analysis technique (Houra et al., 2000; Houra and Nagano, 2006).

The temperature fluctuations, $\hat{\theta}$, mainly associate with the streamwise velocity fluctuations, $\hat{u}$, and the high correlations, $\hat{u}\hat{\theta}$, are maintained for a long period, as seen at the time period (b). On the other hand, the wall-normal heat flux, $-\hat{v}\hat{\theta}$, occurs intermittently, because it mainly associates with high-frequency $Q4$-motions.

3.3. Multi-point measurement results

In order to elucidate the effects of the APG on the dynamical processes of turbulent transport in the velocity and thermal fields, we have conducted simultaneous measurements with five identical three-wire probes, each of which consists of an X-type hot wire and a fine cold wire. Fig. 13 shows simultaneously measured temperature signal traces in APG flow. The abscissa is the time normalized by the Taylor time scale at the nearest point from the wall ($y^+ = 20.7$), as in Fig. 11. The two shaded regions labeled (a) and (b), respectively, correspond to the time periods in Fig. 14a and

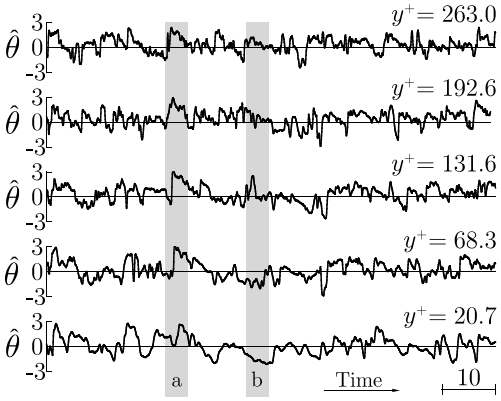

Fig. 13. Simultaneously measured temperature signal traces in APG flow, with time being normalized by Taylor time scale τ_E ($P^+ = 2.56 \times 10^{-2}$).

b. At the time period (a), a cold region with steep positive gradient followed by mild negative gradient in time occurs over the entire area detected by the probe. This large-scale cold region, i.e., cold front, is caused by the strong sweep motion that is frequently observed in APG flow. On the other hand, at the time period (b), a locally hot region elongated in time can be seen at the nearest two points from the wall. This high-temperature region near the wall corresponds to a hot-streak as discussed later.

Next, the turbulence fluctuations of the streamwise and wall-normal velocities and temperature can be reasonably interpolated by using the "proper orthogonal decomposition (POD)" based on the eigenfunctions up to the fifth eigenmode (see Houra et al., 2000). The interpolated turbulence statistics showed good agreement with those obtained by a single three-wire probe. The velocity vectors are depicted with respect to an observer's coordinate moving at a speed of about 0.44 $\overline{U}_e$, which is equal to the mean streamwise velocity at $y^+ \simeq 50$ in the APG flow. Fig. 14a and b show the representative results of velocity vectors and the relevant temperature fluctuations taken at arbitrary times in the APG flow. The vertical axis covers the region from the buffer layer ($y^+ = 20.7$, $y/\delta \simeq 0.04$) to the outside of the log region ($y^+ = 263.0$, $y/\delta \simeq 0.48$). The abscissa is a time period of about 4 τ_E at $y^+ \simeq 50$. The time periods on the abscissa correspond to the shaded regions in Figs. 12, 13, 15 and 16. The solid and broken contour lines represent a hot ($-\theta > 0$) and cold ($-\theta < 0$) region, respectively, and the interval between successive contour lines is $0.05\Delta\overline{\Theta}_e$. The shaded regions represent $|\Delta\overline{\Theta}_e| > 0.05$, and the light and dark regions show hot and cold regions, respectively.

As seen from Fig. 14a, a large-scale sweep motion ($Q4$) with low temperature becomes dominant, ranging from the inner to the outer regions. These predominating patterns can be categorized in the $Q4$–$Q1$–$Q4$ motion (Nagano and Tagawa, 1995; Houra et al., 2000) corresponding to the high-speed cold region frequently observed in the APG flow. On the contrary, Fig. 14b shows the $Q2$–$Q3$–$Q2$ motion associated with an elongated hot region near the wall (i.e., high-temperature low-speed streak). As seen from this figure, the amplitude of the corresponding vectors is relatively small and less active; however, the hot region appears to represent the elongated streaky structure. Thus, the large-amplitude temperature fluctuations are not always associated with strong vertical fluctuations in the APG flow (see the shaded region of (b) in Fig. 12).

3.4. Wavelet analysis of multi-point turbulent signals

Finally, to investigate the local relation between the time and scale of the unique turbulence structures that emerged in the

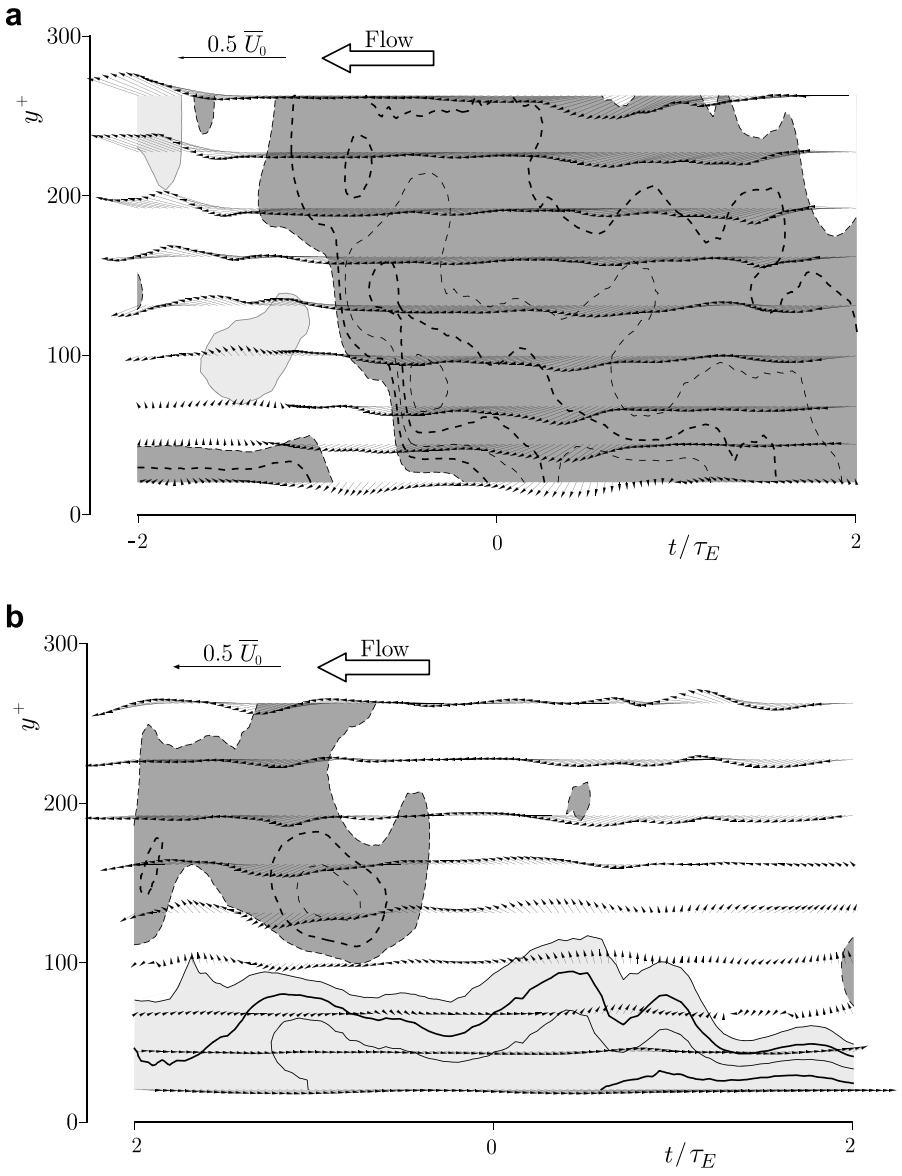

Fig. 14. Instantaneous velocity vectors and relevant temperature fluctuations in APG flow: (a) large-scale sweep motion; (b) near-wall elongated hot region. The solid and broken contour lines represent a hot ($-\theta > 0$) and cold ($-\theta < 0$) region, and the interval between successive contour lines is $0.05\,\Delta\overline{\Theta}_e$.

APG flow, we analyzed the multi-point signals using the continuous wavelet transform. The detailed analysis on the velocity field based on the one-point measurement was shown in our previous paper (Nagano and Houra, 2002), however, here we analyze the multi-point signals in both the velocity and thermal fields for the first time. The one-dimensional continuous wavelet transform of time-series data $X(t)$ is defined (e.g., Farge et al., 1996; Nagano and Houra, 2002) as:

$$W_X(a,t) = \frac{1}{\sqrt{|a|}} \int_{-\infty}^{\infty} X(t')\psi^*\left(\frac{t'-t}{a}\right) \mathrm{d}t' \tag{3}$$

where $\psi(t)$ is an analyzing wavelet, * denotes the complex conjugate, and a is the scaling parameter. As the analyzing wavelet, we adopted the Morlet wavelet,

$$\psi(t) = \mathrm{e}^{\mathrm{i}2\pi k_\psi t}\mathrm{e}^{-t^2/2}, \tag{4}$$

whose Fourier transform is

$$\hat{\psi}(f) = \sqrt{2\pi}\,\mathrm{e}^{-[2\pi(f-k_\psi)]^2/2}. \tag{5}$$

This is a complex-valued function; thus, if we visualize the modulus of the wavelet transform, we can eliminate spurious oscillations of the real part, as recommended by Farge (1992).

If we put $k_\psi = 1$, the scaling parameter, a, corresponds to the inverse of the frequency as $a = 1/f$. Although the Morlet wavelet does not satisfy the following admissibility condition

$$C_\psi = \int_{-\infty}^{+\infty} \frac{|\hat{\psi}(f)|^2}{|f|}\mathrm{d}f < \infty, \tag{6}$$

we used the empirical approximation and estimated the admissibility constant, C_ψ, for the Morlet wavelet,

$$C_\psi = \int_{-\infty}^{\infty} |\hat{\psi}(f)|^2/|f|\mathrm{d}f \simeq \int_{-\infty}^{\infty} |\hat{\psi}(f)|^2\mathrm{d}f = \sqrt{\pi}. \tag{7}$$

We define the wavelet cross-scalogram as

$$E_{XY}(a,t) = W_X^*(a,t)\,W_Y(a,t). \tag{8}$$

If the analyzing wavelet is complex, the cross-scalogram is also complex and can be written in terms of its real and imaginary parts.

$$E_{XY}(a,t) = \mathrm{Co}_{XY}(a,t) - \mathrm{iQuad}_{XY}(a,t). \tag{9}$$

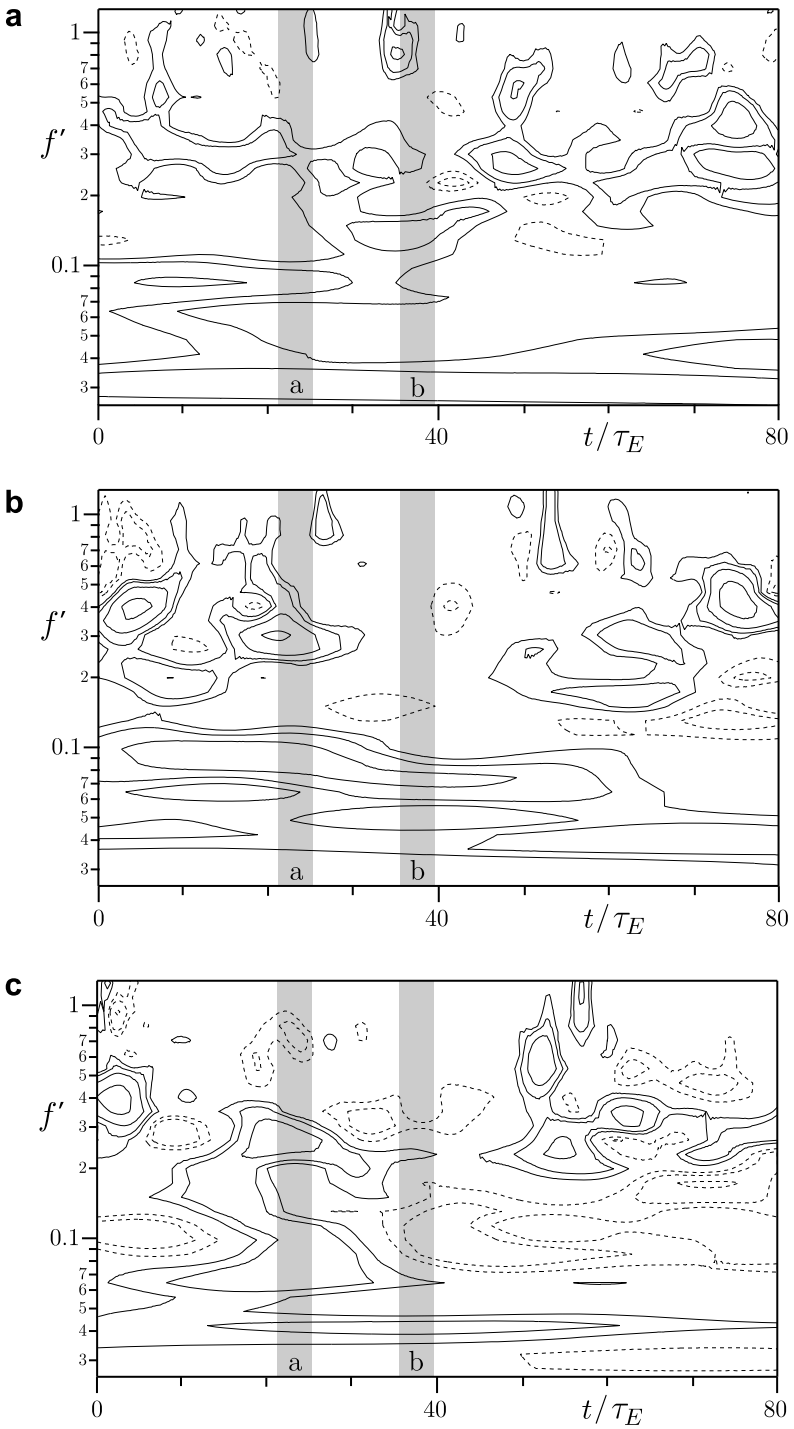

Fig. 15. Simultaneously measured wavelet co-scalograms of $-uv$ in APG flow: (a) $y^+ = 131.6$; (b) $y^+ = 68.3$; (c) $y^+ = 20.7$. The solid and broken contour lines represent positive and negative values, respectively, and the values of the local wavelet spectra are ± 0.05, ± 0.1, ± 0.2 and ± 0.4.

The net contribution to the averaged energy is expressed in real values, and we analyze the wavelet co-scalograms, instead of the cross-scalograms.

The time-averaged value of $E_{XY}(a,t)$ is called the wavelet spectrum $E_{XY}(a)$, and corresponds to the smoothed version of the Fourier spectrum depending on the analyzing wavelet:

$$E_{XY}(a) = \lim_{T\to\infty} \frac{1}{T} \int_{-T/2}^{T/2} E_{XY}(a,t)\mathrm{d}t = \int_{-\infty}^{\infty} P_{XY}(f)|a|\left|\hat{\psi}(af)\right|^2 \mathrm{d}f \tag{10}$$

We take the relation between the second-order moment and the wavelet spectrum as

$$\begin{aligned}\overline{X(t)Y(t)} &= \frac{1}{C_\psi}\int_{-\infty}^{\infty} E_{XY}(a)\frac{\mathrm{d}a}{a^2} \\ &= \frac{1}{C_\psi}\lim_{T\to\infty}\frac{1}{T}\int_{-\infty}^{\infty}\int_{-T/2}^{T/2} E_{XY}(a,t)\mathrm{d}t\frac{\mathrm{d}a}{a^2}.\end{aligned} \tag{11}$$

Thus, if we draw the local wavelet spectrum, $(1/a)E_{XY}(a,t)/C_\psi$, onto the scalogram, it corresponds to the Fourier spectrum multiplied by the frequency. According to spectral theory, the spectral analysis of the second-order moment can only detect interactions from the same frequencies. Thus, we try to extract the information on structures consisting of different positions using the multi-point data obtained in this study.

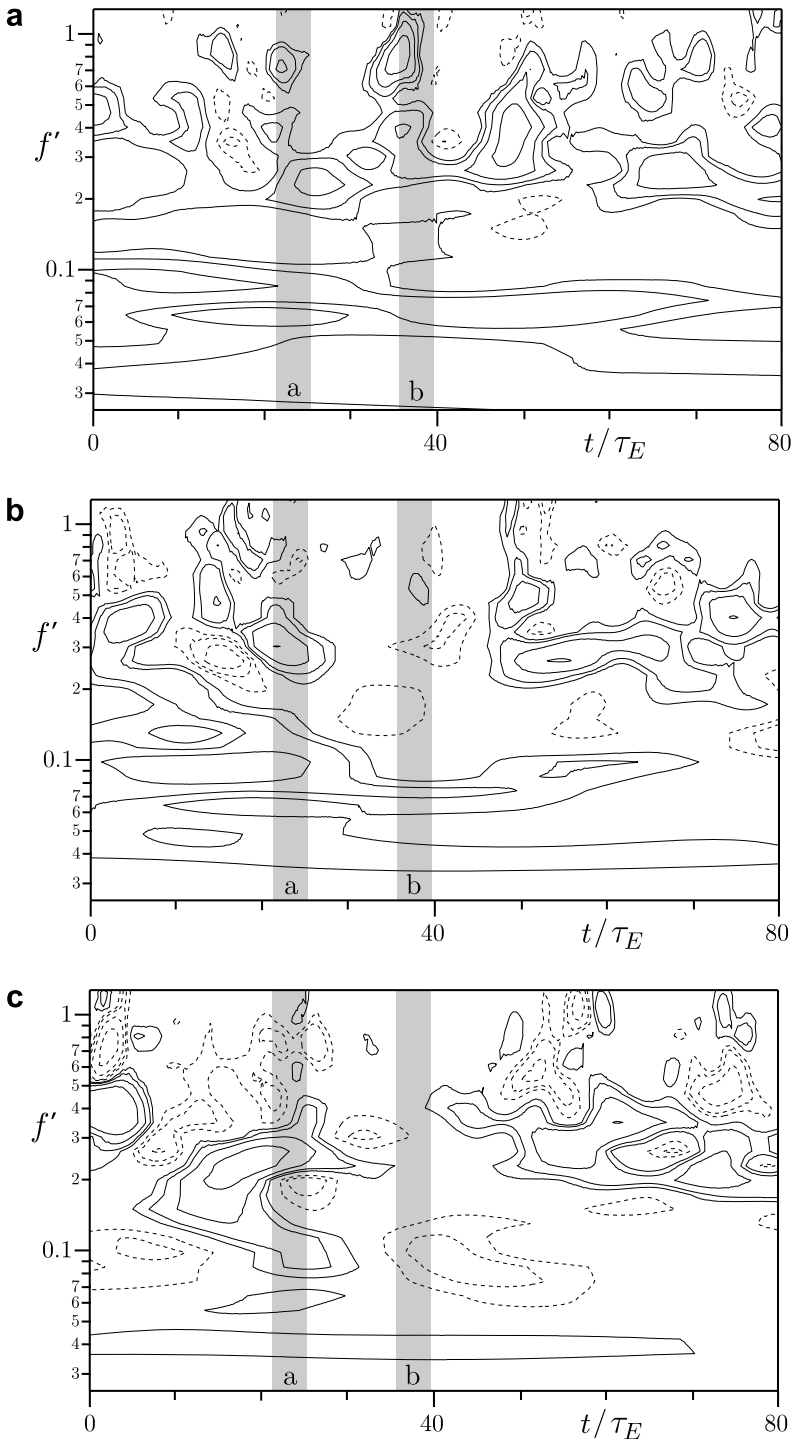

Fig. 16. Simultaneously measured wavelet co-scalograms of $-v\theta$ in APG flow: (a) $y^+ = 131.6$; (b) $y^+ = 68.3$; (c) $y^+ = 20.7$. The solid and broken contour lines represent positive and negative values, respectively, and the values of the local wavelet spectra are ±0.05, ±0.1, ±0.2 and ±0.4.

Figs. 15 and 16, respectively show the wavelet co-scalograms of the Reynolds shear stress, $E_{-uv}(a,t)/(aC_\psi\sqrt{\overline{u^2}}\sqrt{\overline{v^2}})$, and wall-normal heat flux, $E_{-v\theta}(a,t)/(aC_\psi\sqrt{\overline{v^2}}\sqrt{\overline{\theta^2}})$, at the nearest three measured points from the wall, i.e., (a) $y^+ = 131.6$, (b) $y^+ = 68.3$ and (c) $y^+ = 20.7$. The solid and broken contour lines represent positive and negative values, respectively, and the values of the local wavelet spectra are ±0.05, ±0.1, ±0.2 and ±0.4. The abscissa is normalized by the Taylor time scale, as in Fig. 13. The frequency, $f(=a^{-1})$, is also normalized by the Taylor time scale ($f' = f\tau_E$). As seen from these figures, the Reynolds shear stress and the wall-normal heat flux are composed by the contribution from various scales. The local wavelet spectra show large fluctuations in time; thus, the time-averaged characteristics, i.e., the Fourier spectrum, are insufficient to describe the unique feature of the turbulent momentum and heat fluxes.

As seen from Fig. 15, there are slight negative contributions as well as strong positive contributions. The negative contributions frequently observed in the APG flow should be due to the increase in negative contribution to the Reynolds shear stress by the

interaction motions, although the local wavelet spectra of the Reynolds shear stress have almost positive contributions in ZPG flows (for details see Nagano and Houra, 2002). Near the wall, in Figs. 15c and 16c, a large number of negative contributions can be seen, which continue for a long time. Away from the wall, in Figs. 15b and 16b, the distribution of the local wavelet spectrum moves toward the higher-frequency region, and the negative regions are confined to that region.

Next, in order to discuss the spatial extent of the turbulent structures, we examine the wavelet spectra simultaneously measured at various points. The two shaded regions labeled (a) and (b), respectively correspond to the time periods in Fig. 14a and b. During the time period (a), the dominating large-scale sweep motions caused the positive local maximum at $f' \simeq 0.3$. This corresponds to the energy-containing frequency of the wall-normal velocity fluctuation (Nagano et al., 1998). At this frequency the spectra show the positive contribution to both the Reynolds shear stress and the wall-normal heat flux. Thus, it is a typical time period when the dominant sweep motions, contributing to the momentum and heat transfer, are occurring at an energy-containing frequency of the wall-normal velocity fluctuation. On the other hand, during the time period (b), there exist only the very low-frequency motions near the wall. This low-frequency motion shows slightly a negative contribution to both the Reynolds shear stress and wall-normal heat flux. From the results away from the wall (Figs. 15b and 16b), the motions have slightly positive contributions to both fluxes at low-frequency below $f' \simeq 0.1$. In the log region (Figs. 15a and 16a), the high-frequency motion ($f' \simeq 0.8$) has strong energy. This normalized frequency corresponds to the peak frequency of the spectra of $\overline{(\partial u/\partial t)^2}$ (Nagano et al., 1998). This high-frequency motion corresponds to the sweep motions with a cold region above the high-temperature streak as shown in Fig. 14b.

From the above discussion, it is shown that the momentum and heat transports in the APG flow are governed by the motions in various scales widely distributed in time and space. The separation in time scales of turbulent motions near the wall and in the outer regions, conjectured from the one-point measurement results (Houra et al., 2000; Nagano and Houra, 2002), is due to the large-scale structures, as large as the boundary layer thickness, and the small-scale turbulent structures in the near-wall region. From the standpoint of heat transfer, both different-scale motions are important fluid motions in non-equilibrium APG flows.

4. Conclusions

Experimental investigation has been made on a non-equilibrium turbulent boundary layer subjected to adverse pressure gradient developing on a uniformly heated flat wall. The spatio-temporal structures educed from a multi-point simultaneous measurement technique are presented. Then, the energy-containing events in the near-wall region are discussed based on the results of the wavelet analysis. From the observation of the instantaneous velocity vectors and temperature fluctuations obtained from the proper orthogonal decomposition (POD), it is found that in the near-wall region, elongated hot regions stay dull and less active; on the other hand, large-scale cold regions having strong energy frequently intrude into the near-wall region.

Acknowledgements

This work was partially supported by Grant-in-Aid for Scientific Research (S) (No. 17106003) from the Japan Society for the Promotion of Science (JSPS), and Young Scientists (B) (No. 19760134) from the Ministry of Education, Culture, Sports, Science and Technology (MEXT).

References

Antonia, R.A., Krishnamoorthy, L.V., Fulachier, L., 1988. Correlation between the longitudinal velocity fluctuation and temperature fluctuation in the near-wall region of a turbulent boundary layer. Int. J. Heat Mass Transfer 31, 723–730.

Blackwell, B.F., Kays, W.M., Moffat, R.J., 1972. The turbulent boundary layer on a porous plate: an experimental study on the heat transfer behavior with adverse pressure gradients. Thermosciences Div. Department of Mechanical Engineering, Stanford University, Report HMT-16, Stanford, CA.

Bradshaw, P., 1967. The turbulence structure of equilibrium boundary layers. J. Fluid Mech. 29, 625–645.

Bradshaw, P., Huang, P.G., 1995. The law of the wall in turbulent flow. Proc. R. Soc. Lond., A 451, 165–188.

Clauser, F.H., 1954. Turbulent boundary layers in adverse pressure gradients. J. Aero. Sci. 21, 91–108.

Coleman, G.N., Kim, J., Spalart, P.R., 2003. Direct numerical simulation of a decelerated wall-bounded turbulent shear flow. J. Fluid Mech. 495, 1–18.

Debisschop, J.R., Nieuwstadt, F.T.M., 1996. Turbulent boundary layer in an adverse pressure gradient: effectiveness of riblets. AIAA J. 34, 932–937.

Farge, M., 1992. Wavelet transforms and their applications to turbulence. Annu. Rev. Fluid Mech. 24, 395–457.

Farge, M., Kevlahan, N., Perrier, V., Goirand, É., 1996. Wavelets and turbulence. Proc. IEEE 84, 639–669.

Hishida, M., Nagano, Y., 1978. Simultaneous measurements of velocity and temperature in nonisothermal flows. Trans. ASME, J. Heat Transfer 100, 340–345.

Hishida, M., Nagano, Y., 1988a. Turbulence measurements with symmetrically bent V-shaped hot-wires. Part 1. Principles of operation. Trans. ASME, J. Fluid Eng. 110, 264–269.

Hishida, M., Nagano, Y., 1988b. Turbulence measurements with symmetrically bent V-shaped hot-wires. Part 2. Measuring velocity components and turbulent shear stresses. Trans. ASME, J. Fluid Eng. 110, 270–274.

Houra, T., Nagano, Y., 2006. Effects of adverse pressure gradient on heat transfer mechanism in thermal boundary layer. Int. J. Heat Fluid Flow 27, 967–976.

Houra, T., Tsuji, T., Nagano, Y., 2000. Effects of adverse pressure gradient on quasi-coherent structures in turbulent boundary layer. Int. J. Heat Fluid Flow 21, 304–311.

Indinger, T., Buschmann, M.H., Gad-el-Hak, M., 2006. Mean-velocity profile of turbulent boundary layers approaching separation. AIAA J. 44, 2465–2474.

Le, H., Moin, P., Kim, J., 1997. Direct numerical simulation of turbulent flow over a backward-facing step. J. Fluid Mech. 330, 349–374.

Lee, J.-H., Sung, H.J., 2007. Effects of Adverse pressure gradient on a turbulent boundary layer. In: Proceedings of the Fifth International Symposium on Turbulence and Shear Flow Phenomena, TU München, Garching, Germany, August 27–29, pp. 29–34.

Lueptow, R.M., Breuer, K.S., Haritonidis, J.H., 1988. Computer-aided calibration of X-probes using a look-up table. Exp. Fluids 6, 115–118.

Na, Y., Moin, P., 1996. Direct Numerical Simulation of Turbulent Boundary Layers with Adverse Pressure Gradient and Separation. Stanford University, Rept. TF-68.

Nagano, Y., Houra, T., 2002. Higher-order moments and spectra of velocity fluctuations in adverse-pressure-gradient turbulent boundary layer. Exp. Fluids 33, 22–30.

Nagano, Y., Tagawa, M., 1995. Coherent motions and heat transfer in a wall turbulent shear flow. J. Fluid. Mech. 305, 127–157.

Nagano, Y., Tagawa, M., Tsuji, T., 1993. Effects of adverse pressure gradients on mean flows and turbulence statistics in a boundary layer. In: Durst, F., Friedrich, R., Launder, B.E., Schmidt, F.W., Schumann, U., Whitelaw, J.H. (Eds.), Turbulent Shear Flows, vol. 8. Springer-Verlag, Berlin.

Nagano, Y., Tsuji, 1994. Recent developments in hot- and cold-wire techniques for measurements in turbulent shear flows near walls. Exp. Therm. Fluid Sci. 9, 94–110.

Nagano, Y., Tsuji, T., Houra, T., 1998. Structure of turbulent boundary layer subjected to adverse pressure gradient. Int. J. Heat Fluid Flow 19, 563–572.

Perry, A.E., Bell, J.B., Joubert, P.N., 1966. Velocity and temperature profiles in adverse pressure gradient turbulent boundary layer. J. Fluid Mech. 25, 299–320.

Rotta, J.C., 1962. Turbulent boundary layers in incompressible flow. Prog. Aero. Sci. 2, 1–221.

Samuel, A.E., Joubert, P.N., 1974. A boundary layer developing in an increasingly adverse pressure gradient. J. Fluid Mech. 66, 481–505.

Skåre, P.E., Krogstad, P.-Å., 1994. A turbulent equilibrium boundary layer near separation. J. Fluid Mech. 272, 319–348.

Skote, M., Henningson, D.S., Henkes, R.A.W.M., 1998. Direct numerical simulation of self-similar turbulent boundary layers in adverse pressure gradients. Flows Turbul. Combus. 60, 47–85.

Spalart, P.R., 1988. Direct simulation of a turbulent boundary layer up to $R_\theta = 1410$. J. Fluid Mech. 187, 61–98.

Spalart, P.R., Watmuff, J.H., 1993. Experimental and numerical study of a turbulent boundary layer with pressure gradients. J. Fluid Mech. 249, 337–371.

Tagawa, M., Tsuji, T., Nagano, Y., 1992. Evaluation of X-probe response to wire separation for wall turbulence measurements. Exp. Fluids 12, 413–421.
Townsend, A.A., 1976. The Structure of Turbulent Shear Flow, second ed. Cambridge University Press. p. 298.
Verriopoulos, C.A., 1983. Effects of Convex Surface Curvature on Heat Transfer in Turbulent Flow. Ph.D Thesis, Imperial College.
Volino, R.J., Simon, T.W., 1997. Velocity and temperature profiles in turbulent boundary layer flows experiencing streamwise pressure gradients. Trans. ASME, J. Heat Transfer 119, 433–439.
Wang, X., Castillo, L., Araya, G., 2008. Temperature scalings and profiles in forced convection turbulent boundary layers. Trans. ASME, J. Heat Transfer 130, 021701 (17 pp.).